ACS APPLIED MATERIALS & INTERFACES

www.acsami.org

Research Article

Facile Synthesis of $ZnMn_2O_4$@rGO Microspheres for Ultrasensitive Electrochemical Detection of Hydrogen Peroxide from Human Breast Cancer Cells

Yuanyuan Li, Ke Huan, Dongmei Deng,* Li Tang, Jinhua Wang, and Liqiang Luo*

Cite This: *ACS Appl. Mater. Interfaces* 2020, 12, 3430−3437

Read Online

ACCESS | Metrics & More | Article Recommendations | Supporting Information

ABSTRACT: Mixed transition-metal oxides have witnessed increasing attention in catalysts and electrocatalysts. Herein, reduced graphene oxide-wrapped $ZnMn_2O_4$ microspheres ($ZnMn_2O_4$@rGO) were facilely synthesized through the solvothermal technique. The microstructure and morphology of $ZnMn_2O_4$@rGO microspheres were analyzed under Raman, X-ray photoelectron, X-ray diffraction, and energy-dispersive spectroscopies and scanning electron microscopy. The synthesized $ZnMn_2O_4$@rGO was employed as an excellent electrocatalyst for the reduction of hydrogen peroxide (H_2O_2). The $ZnMn_2O_4$@rGO-modified glassy carbon electrode ($ZnMn_2O_4$@rGO/GCE) exhibited a linear detection to H_2O_2 in a wide concentration range of 0.03−6000 μM with a detection limit of 0.012 μM. The biosensor was evaluated to determine H_2O_2 secreted by human breast cancer cells (MCF-7), indicating its promising applications in physiology and diagnosis.

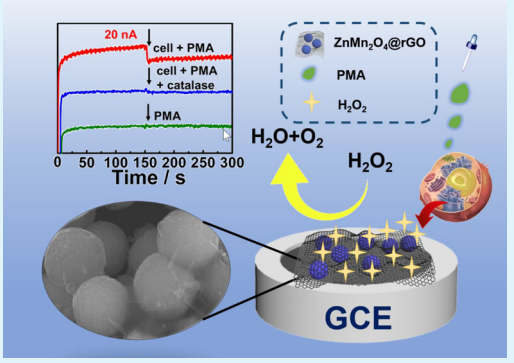

KEYWORDS: *$ZnMn_2O_4$@rGO, microspheres, solvothermal, hydrogen peroxide, electrochemical sensor, breast cancer cells*

1. INTRODUCTION

As a significant type of reactive oxygen, H_2O_2 is not only an indispensable substance in chemical and food industries but also an indicator of oxidative stress associated with the pathological and physiological events including memory functions, brain injury, aging, and cancer.[1−3] According to the American Cancer Society, more than 255,000 new cases of breast cancer were diagnosed, representing 15.3% of all new cancer cases in the U.S. in 2018.[4] Efforts to enhance the efficiency of early diagnosis and therapy are important ways to reducing the risk and mortality rate.[5] Actually, an increasing number of evidences reveal that H_2O_2 plays an important role in regulating pathways in tumor cell survival.[6] Accordingly, reliable, rapid, and quantitative quantification of H_2O_2 is absolutely necessary in clinical and bioanalytical chemistry. In recent years, many technologies including electrochemistry, chemiluminescence, fluorimetry, spectrophotometry, and titrimetry methods[7−9] have been used to detect H_2O_2. Among them, electrochemical techniques have gained intensive interest in biological applications owing to their superiorities including high sensitivity and selectivity, good performance, and convenient operation. Moreover, it is an efficient way to further understand the dynamic release process of H_2O_2.

Various electrochemical sensors have been reported in which enzyme-involved biosensors can make sure of excellent selectivity. Nevertheless, the instability, complexity of immobilization, and high cost restrict their usages. In comparison with enzyme-based biosensors, nonenzymatic sensors based on transition-metal oxides have achieved increasing interest, including $NiFe_2O_4$,[10] MnO_2,[11] ZnO,[12] Cu_2O/Cu,[13] and Fe_3O_4.[14] Among them, mixed transition-metal oxides possess higher electrochemical performance than monocomponent metal oxides due to their great flexibility of the structure, excellent electrochemical capacitance, and low costs.[15−17] Balasubramanian et al. reported a solvothermal technique to synthesize Mn_2CuO_4 microspheres. The as-prepared Mn_2CuO_4 showed good catalytic activity to H_2O_2 with a detection limit of 13 nM, which was utilized to the detection of living cell H_2O_2.[18] Wu et al. presented that Mn_3O_4−$MnCo_2O_4$ nanoparticles gave superior electrocatalysis for H_2O_2 sensing.[19] However, the weak conductivity hinders their practical applications.

Graphene is a 2D carbon matrix, as a new class of carbon-based nanomaterial sheet with a single layer, that can support metal or transition-metal oxides for its ability of quick electron transfer,[20−22] large surface area,[23] and superior structural flexibility.[24] There are lots of functional groups such as epoxy, carboxyl, and hydroxyl groups on the surface of graphene oxide, which can improve its dispersibility and hydrophilicity.[25]

Received: October 23, 2019
Accepted: December 26, 2019
Published: December 26, 2019

Recently, graphene oxide-based material-modified electrochemical H_2O_2 sensors have become an interesting research topic.[26−28]

In our previous work, spinel-type $ZnMn_2O_4$ microspheres have been solvothermally synthesized for nonenzymatic electrocatalysis of H_2O_2.[29] However, due to the weak conductivity of $ZnMn_2O_4$ microspheres, the detection limit for H_2O_2 is not low enough. In other words, more effort is needed to develop materials with better conductivity and sensitivity for their bioelectrocatalytical applications. Considering the unique property in surface area, conductivity, and biocompatibility, graphene is considered an ideal candidate to functionalize $ZnMn_2O_4$. In this work, rGO-wrapped $ZnMn_2O_4$ ($ZnMn_2O_4$@rGO) microspheres were fabricated using the solvothermal approach. The synthesized $ZnMn_2O_4$@rGO showed enhanced electrocatalytic ability to the reduction of H_2O_2. Furthermore, the proposed sensor was applied to monitor H_2O_2 in breast cancer cells.

2. EXPERIMENTAL SECTION

2.1. Apparatus. The morphology of $ZnMn_2O_4$@rGO was investigated under SEM (JEOL JSM-6700F) with an EDS (energy-dispersive spectroscopy) analyzer at 20 kV. For the collection of the crystallinity of the product in the range of 10−70°, XRD (Rigaku DLMAX-2200) was employed. With the use of ESCA spectrometer (Thermo Scientific), XPS spectra were conducted with an Al Kα radiation source. Raman spectroscopy was performed using a Renishaw in Via Reflex with 633 nm at ambient temperature (INVIA, England). The electrochemical measurements were recorded on a CHI 1030c electrochemical analyzer (CHI, China) fitted by the traditional three-electrode system including a platinum foil, Ag/AgCl (saturated KCl), and the modified glassy carbon electrode (GCE). Image acquisition was carried out using a BM-37XCS invert biological microscope (BM, China).

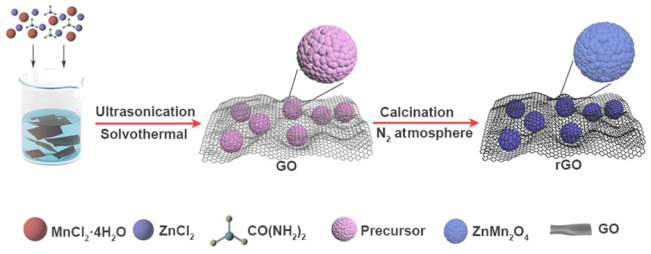

Figure 1. Schematic diagram of the major steps for the synthesis of $ZnMn_2O_4$@rGO.

2.2. Reagents and Chemicals. Sinopharm (China) provided $MnCl_2·4H_2O$, NaOH, ethylene glycol, urea, $ZnCl_2$, and H_2O_2 solution (30%). Sigma (USA) provided graphene oxide (GO), glycine (Gly), citric acid (CA), uric acid (UA), citric acid (AA), dopamine (DA), β-D(+) glucose (Glu), phorbol (PMA), and catalase (2000−5000 U mg^{-1}). All chemicals belonged to the analytical level. Ultrapure deionized water was employed during experiments.

2.3. Synthesis of $ZnMn_2O_4$@rGO. At first, 40 mL of GO dispersion (approximately 1.5 mg mL^{-1}) was dispersed in ethylene glycol with ultrasonication for 30 min. To this dispersion, 4.497 mmol of $ZnCl_2$ and 2.002 mmol of $MnCl_2·4H_2O$ were added and ultrasonicated for another 30 min. Then, 4.995 mmol of urea was added into the mixture under vigorous stirring. Next, the solution was placed in a Teflon-lined autoclave for the reaction at 200 °C for 24 h. The filtered samples were cleaned with water and ethanol repeatedly and then dried at 60 °C overnight in the case of vacuum. Finally, the final powder underwent the calcining process at 500, 600, and 700 °C for 2 h in a N_2 atmosphere. For comparison, pure $ZnMn_2O_4$ microspheres without rGO were synthesized. The synthesis process is illustrated in Figure 1.

2.4. Fabrication of $ZnMn_2O_4$@rGO/GCE. With the use of Buehler polishing kit, the GCE underwent polishing carefully with alumina powder. After ultrasonication in absolute water and alcohol separately for 3 min to remove any dirt attached to its surface, the GCE was kept at ambient temperature to dry. Subsequently, 5 μL of

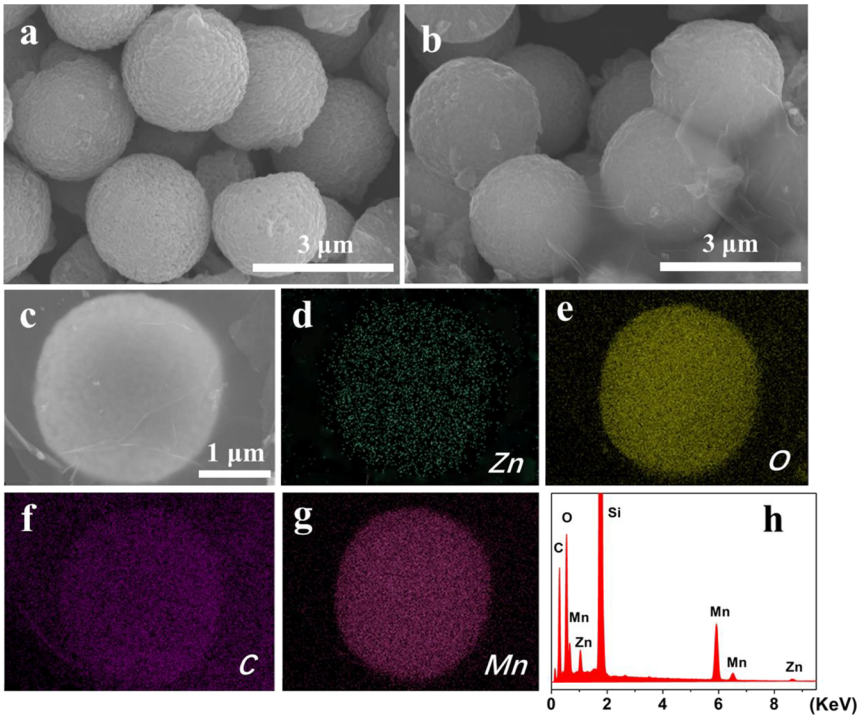

Figure 2. (a) SEM image of $ZnMn_2O_4$. (b) SEM image of $ZnMn_2O_4$@rGO. (c−g) Elemental mapping images of $ZnMn_2O_4$@rGO and corresponding elemental mapping images of Zn, O, C, and Mn, respectively. (h) EDS spectrum. The peak of Si is from the Si grid.

https://dx.doi.org/10.1021/acsami.9b19126
ACS Appl. Mater. Interfaces 2020, 12, 3430−3437

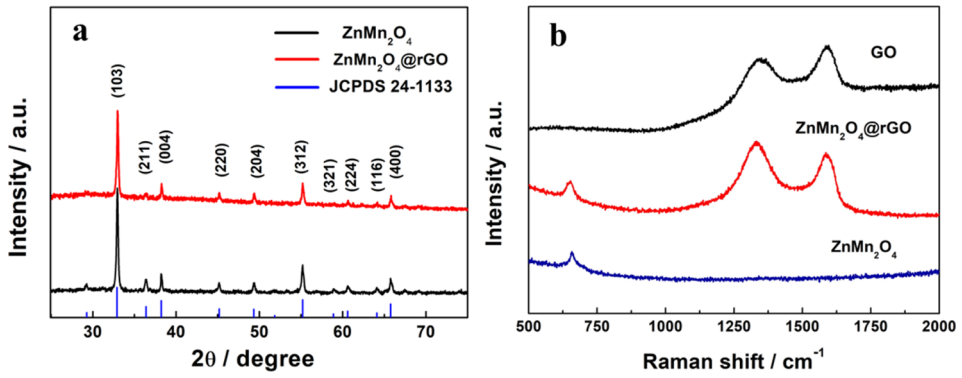

Figure 3. (a) XRD patterns of $ZnMn_2O_4$ and $ZnMn_2O_4$@rGO. (b) Raman spectra of GO, $ZnMn_2O_4$, and $ZnMn_2O_4$@rGO.

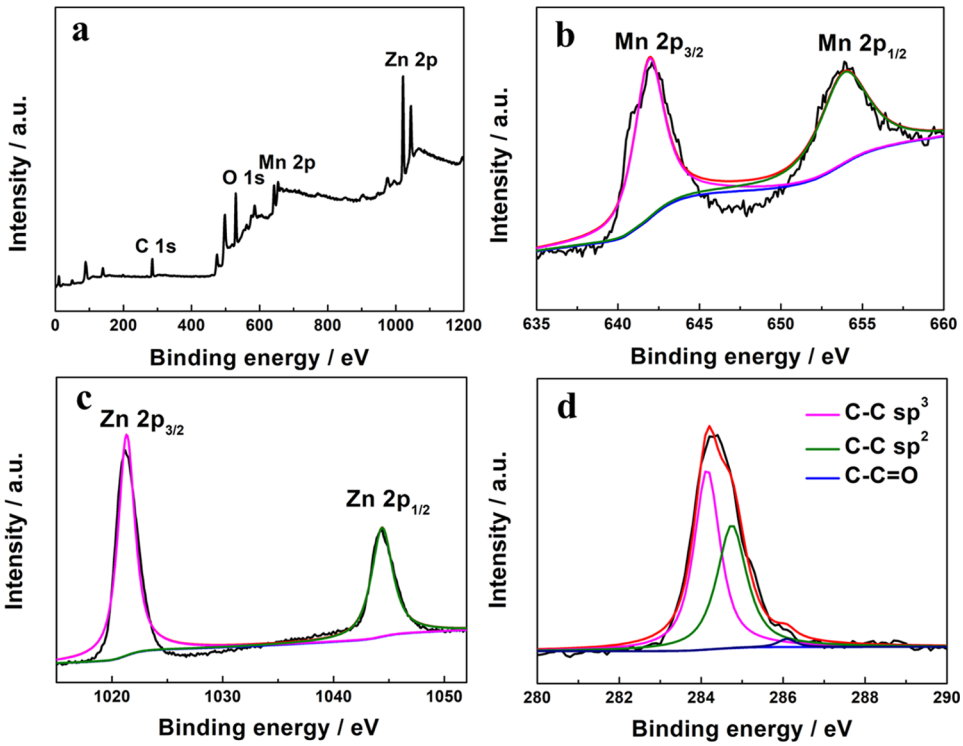

Figure 4. XPS spectra of ZnMn2O4@rGO. (a) Full wide-scan, (b) Mn 2p, (c) Zn 2p, and (d) C 1s spectra.

$ZnMn_2O_4$@rGO microspheres in water was cast on the GCE to prepare $ZnMn_2O_4$@rGO/GCE.

2.5. Detection of Extracellular H_2O_2. MCF-7 cells were kindly provided by School of Life Science, Shanghai University. In a humidified incubator (5% CO_2 + 95% air), the cells were cultured in RPMI-1640 and 10% fetal bovine serum at 37 °C. The preparation process of MCF-7 cells for electrochemical measurements was according to the previous work of our group.[30] Finally, a concentration of 6 × 106 cells mL^{-1} for the real-time detection of H_2O_2 was achieved. For the detection of released H_2O_2 from MCF-7, 10 μL (5.0 μg mL^{-1}) of PMA was dropped into the solution containing cells. Then, the suspension was redispersed in 0.2 M NaOH for electrochemical measurements.

3. RESULTS AND DISCUSSION

3.1. SEM and EDS Characterization. In this work, $ZnMn_2O_4$@rGO microspheres were synthesized by the one-step solvothermal approach. Especially, the effect of temperature on calcinations was studied at different temperatures of 500, 600, and 700 °C for 2 h in a N_2 atmosphere. SEM results indicated that $ZnMn_2O_4$@rGO microspheres calcined at 600 °C (Figure 2b) exhibited better morphology that those at 500 and 700 °C (Figure S1). For pure $ZnMn_2O_4$, Figure 2a shows a sphere-like morphology with a rough surface on the microspheres. From Figure 2b, $ZnMn_2O_4$@rGO revealed similar sizes but less coarse surfaces than those of $ZnMn_2O_4$. In addition, the rGO films not only wrapped or covered $ZnMn_2O_4$ microspheres but also filled the space between $ZnMn_2O_4$, thus significantly linking to the adjacent $ZnMn_2O_4$ microspheres. Such a unique structure can expedite electron transport in the contact area of $ZnMn_2O_4$ microspheres and form a feasible percolating network, thereby enhancing the electrocatalytic performance. EDS was performed to further identify the chemical composition of the $ZnMn_2O_4$@rGO composites. From Figure 2c–g, EDS mapping revealed homogeneous distribution of Zn, O, C, and Mn in the $ZnMn_2O_4$@rGO microsphere, confirming that the $ZnMn_2O_4$ microspheres were well wrapped by chiffon-like rGO nanosheets. From EDS analysis (Figure 2h), the presence of Zn, Mn, C, and O was conformed. Additionally, the atomic ratio of Zn/Mn was 1:2 from quantitative EDS analysis, which was the

https://dx.doi.org/10.1021/acsami.9b19126
ACS Appl. Mater. Interfaces 2020, 12, 3430−3437

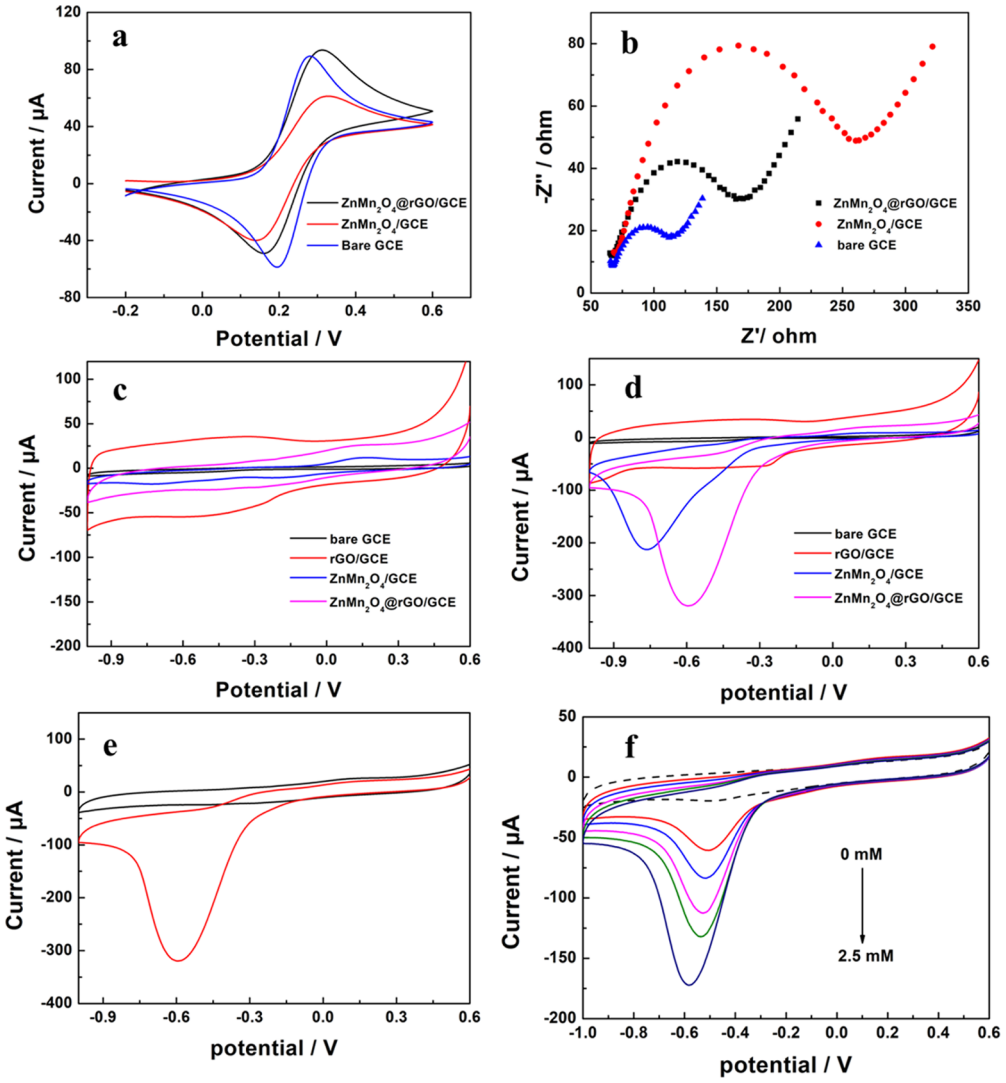

Figure 5. (a) CVs and (b) EIS recorded in 5.0 mM $[Fe(CN)_6]^{3-/4-}$ + 0.1 M KCl at the GCE, $ZnMn_2O_4$/GCE, and $ZnMn_2O_4$@rGO/GCE. CVs of the bare GCE, rGO/GCE, $ZnMn_2O_4$/GCE, and $ZnMn_2O_4$@rGO/GCE in the (c) absence and (d) presence of 5 mM H_2O_2. (e) CVs of $ZnMn_2O_4$@rGO/GCE in the absence and presence of 5 mM H_2O_2. (f) CVs of $ZnMn_2O_4$@rGO/GCE with different concentrations of H_2O_2 in 0.2 M NaOH at a scan rate of 100 mV s^{-1}.

typical chemical composition of zinc manganese spinel. Moreover, the C peak of $ZnMn_2O_4$@rGO presents a high intensity, suggesting the presence of rGO.

3.2. XRD, Raman, and XPS Spectroscopy Characterization. The crystallinity of $ZnMn_2O_4$@rGO was studied by XRD. From Figure 3a, the diffraction peaks are obvious. Characteristic reflection peaks at 2θ = 29.3, 33.03, 36.3, 59.01, 60.77, and 65.1° belong to (112), (103), (211), (224), and (400) phase structures of $ZnMn_2O_4$, separately. Obviously, the synthesized $ZnMn_2O_4$@rGO composites exhibited high crystallinity based on the small peak width and large peak intensity. Moreover, the presence of rGO in $ZnMn_2O_4$ did not impact the formation of the spinel cubic phase.

Figure 3b presents Raman spectra of $ZnMn_2O_4$, $ZnMn_2O_4$@rGO, and GO, which were recorded from 500 to 2000 cm^{-1}. In the Raman spectra of $ZnMn_2O_4$ and $ZnMn_2O_4$@rGO, the obvious peaks at 660 cm^{-1} belonged to the characteristic vibration modes of $ZnMn_2O_4$.[31−34] In the spectrum of $ZnMn_2O_4$@rGO composite, peaks appearing at 1332 and 1585 cm^{-1} resulted from the presence of disordered (D) and graphitic (G) bands of rGO, respectively. In the Raman spectrum of GO, I_D/I_G was ∼0.84, while in $ZnMn_2O_4$@rGO, the I_D/I_G in the spectrum was found to be ∼1.09. The increase in I_D/I_G of $ZnMn_2O_4$@rGO clearly shows the removal of oxygen functional groups in GO.[35,36]

XPS analysis was applied to reveal electronic configuration of $ZnMn_2O_4$@rGO composite. In the survey spectrum (Figure 4a), the characteristic peaks of zinc, manganese, carbon, and oxygen elements are obvious.[34] In Mn 2p spectra (Figure 4b), the peaks at 642.6 and 654.4 eV were attributed to Mn $2p_{3/2}$ and Mn $2p_{1/2}$, respectively. The binding energy separation was 11.8 eV, in accordance with that of $ZnMn_2O_4$.[36,37] The two peaks at 1021.4 and 1044.3 eV in Zn 2p spectra (Figure 4c) were assigned to Zn $2p_{3/2}$ and Zn $2p_{1/2}$, respectively.[38−41] The C 1s XPS spectra of $ZnMn_2O_4$@rGO are given in Figure 4d. The peaks at 284.7 and 285.7 eV could be observed, which were ascribed to the C−C sp^2 and C−C sp^3, respectively, confirming the reduction of GO to rGO in the course of heat treatment.[42−44]

3.3. Electrochemical Studies. To monitor the interfacial behavior of the modified electrodes, cyclic voltammetry (CV) and electrochemical impedance spectroscopy (EIS) measure-

https://dx.doi.org/10.1021/acsami.9b19126
ACS Appl. Mater. Interfaces 2020, 12, 3430−3437

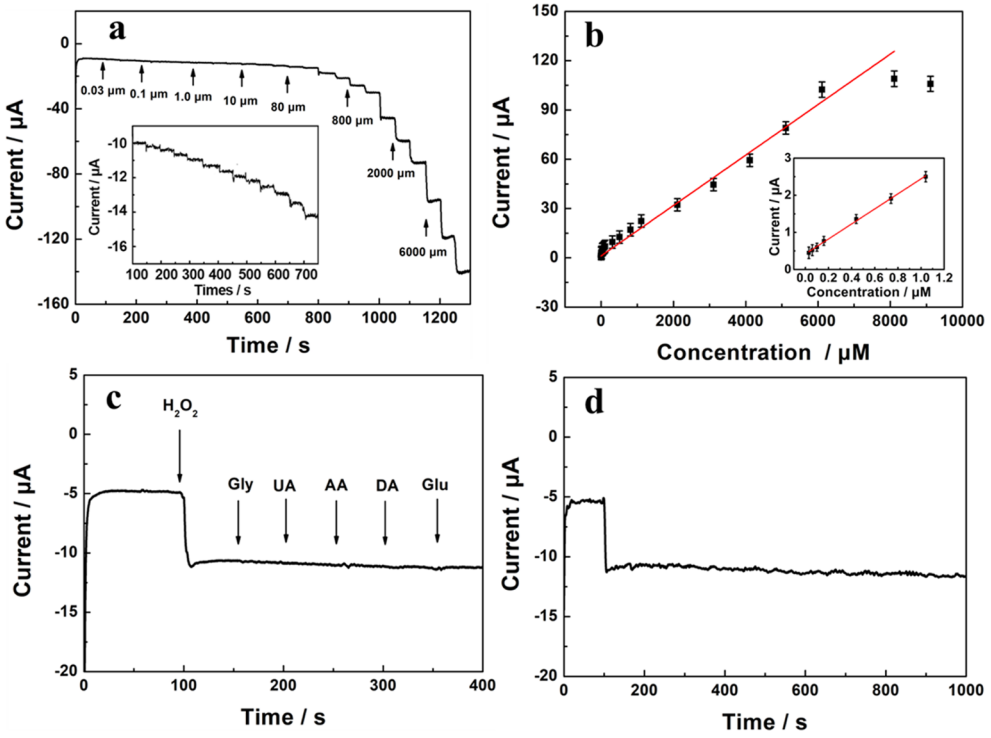

Figure 6. (a) Amperometric response of $ZnMn_2O_4$@rGO/GCE for different concentrations of H_2O_2 in 0.2 M NaOH at an applied potential of −0.6 V. (b) Corresponding calibration curve. Inset is the linearity for low concentrations. (c) Amperometric response of $ZnMn_2O_4$@rGO/GCE to 0.5 mM H_2O_2 and different interferences in stirring 0.2 M NaOH at an applied potential of −0.6 V. (d) Current change of $ZnMn_2O_4$@rGO/GCE to 0.5 mM H_2O_2 during the 1000 s test period in 0.2 M NaOH at an applied potential of −0.6 V.

Table 1. Comparison of Property between the Proposed Sensor and Other H_2O_2 Sensors

modified material	linear range (μM)	detection limit (μM)	reference
PdPtNCs[a]@SnO_2GN[b]	1−300	0.3	47
MnO_2/Co_3O_4/graphene	5−1200	0.8	48
Pt-ZnO nanotube	20−5000	1.5	49
Pt/Fe_3O_4/rGO	100−2400	1.58	50
NiO/α-Fe_2O_3	500−3000	50	51
AgNPs[c]-NCNTs[d]	1−11,000	0.03	52
Cu_2O/Ag	50−500	4.0	53
MoS_2-Au	0.5−200	0.1	54
Fe_3O_4@Ag	0.5−20	0.16	55
myoglobin/$MnMoSe_2$	0.09−60	0.004	56
$ZnMn_2O_4$@rGO	0.03−6000	0.012	this work

[a]Nanocages. [b]Graphene nanosheets. [c]Nanoparticles. [d]N-doped carbon nanotubes.

ments were employed. As depicted in Figure 5a, compared to the bare GCE, redox peak currents at $ZnMn_2O_4$/GCE were lower accompanied with a larger difference in peak potentials, demonstrating poor conductivity of the $ZnMn_2O_4$ composite. However, the peak currents at $ZnMn_2O_4$@rGO/GCE increased dramatically, and the difference in peak potentials decreased, indicating that rGO can enhance the electroconductivity of the biosensor. In addition, EIS was applied to characterize the modified electrodes. Generally, the semicircle part of the Nyquist plot in EIS is in accordance with the electron transfer restricted process in which the diameter reveals the electron transfer resistance (R_{et}).[45] Compared to the R_{et} of the bare electrode (46.4 Ω), the R_{et} of $ZnMn_2O_4$/GCE increased to 192.3 Ω. However, the R_{et} value obtained at $ZnMn_2O_4$@rGO/GCE decreased remarkably to 99.1 Ω (Figure 5b). The EIS results further confirm that rGO can enhance the electroconductivity of the biosensor.

Figure 5c,d illustrates the CVs of the bare GCE, rGO/GCE, $ZnMn_2O_4$/GCE, and $ZnMn_2O_4$@rGO/GCE in the absence and presence of 5 mM H_2O_2. From Figure 5c, no electrochemical response could be observed at the bare GCE. However, after being modified by rGO, a higher background current was observed obviously, revealing easier electron transfer and more electroactive surface area provided by rGO. The $ZnMn_2O_4$@rGO/GCE demonstrated the maximum current due to the fact that $ZnMn_2O_4$@rGO microspheres offered the largest active surface and effective conduction channels. After addition of 5 mM H_2O_2 (Figure 5d), the bare GCE exhibited no obvious current response, but a slight peak could be observed for the electroreduction of H_2O_2 at rGO/GCE, which was driven from the improved electroconductivity of rGO, whereas electroreduction of H_2O_2 was triggered at $ZnMn_2O_4$/GCE. Clearly, the $ZnMn_2O_4$@rGO/GCE exhibited the largest peak current toward the electroreduction of H_2O_2 (Figure 5c), indicating that the synthesized $ZnMn_2O_4$@rGO microspheres could create much more active sites for the H_2O_2 molecule adsorption and reaction, thus improving electrocatalytic ability to H_2O_2 reduction. Moreover, compared to that of $ZnMn_2O_4$/GCE, the peak potential for H_2O_2 reduction on $ZnMn_2O_4$@rGO/GCE shifted from −0.8 to −0.6 V, resulting from the synergistic effects of $ZnMn_2O_4$ and rGO. From Figure 5d, the peak current increased with the increase of H_2O_2 concentration, suggesting that H_2O_2 had been successfully electrocatalyzed on $ZnMn_2O_4$@rGO over a wide concentration window. The electroreduction mechanism of H_2O_2 on

https://dx.doi.org/10.1021/acsami.9b19126
ACS Appl. Mater. Interfaces 2020, 12, 3430−3437

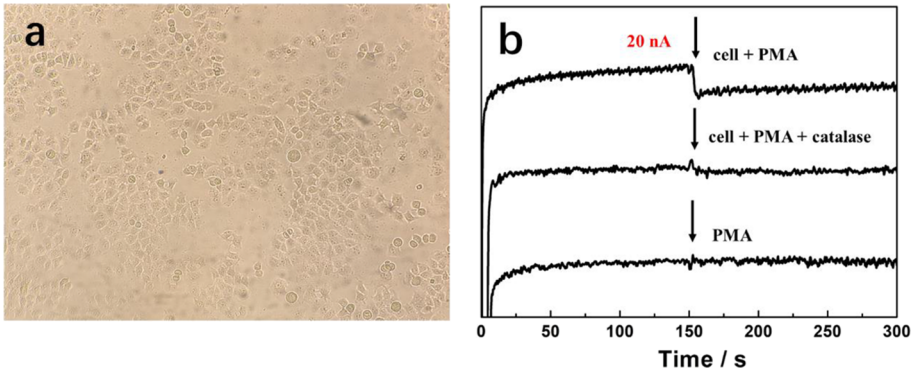

Figure 7. (a) Microscopy images of MCF-7 cells. (b) Amperometric responses obtained at the $ZnMn_2O_4$@rGO/GCE in the absence and presence of MCF-7 with the addition of 10.0 mg mL^{-1} PMA and 400 U mL^{-1} catalase.

the modified electrode in the alkaline electrolyte is similar to $(Mn, Co)_3O_4$.[29,46] Moreover, the electrode kinetics toward H_2O_2 electroreduction suggested that the electrochemical process acted as a surface-controlled process (see the Supporting Information, Figure S2).

3.4. Amperometric Detection, Selectivity, and Stability. Experimental parameters, which could affect the electrochemical performance of the H_2O_2 sensor, were optimized. According to the analysis of electrochemical test results, the obtained optimal conditions were 0.2 M NaOH, −0.6 V, and 12.0 mg mL^{-1} $ZnMn_2O_4$@rGO, separately (see the Supporting Information, Figure S3). Under optimal conditions, a typical chronoamperometric response with successively injecting different concentrations of H_2O_2 on $ZnMn_2O_4$@rGO/GCE is shown in Figure 6a. The electrochemical response was linear with H_2O_2 concentrations from 0.03 to 6000 μM (Figure 6b), and the regression equation was I (μA) = 2.728 + 0.015C (μM) (R^2 = 0.995). The detection limit was assessed as 0.012 μM, and the sensitivity was 1121 μA mM^{-1} cm^{-2}. Comparison of $ZnMn_2O_4$@rGO/GCE with other H_2O_2 biosensors is presented in Table 1, showing that our biosensor exhibits prominent electrocatalytic performance for H_2O_2 reduction.

Anti-interference ability is a critical property indicator for nonenzymatic biosensors. Some electroactive substances, especially DA and AA, normally coexist with H_2O_2 in human samples. They may affect the current response during the detection of H_2O_2. From Figure 6c, no obvious interference was observed for the detection of 0.5 mM H_2O_2 after adding Gly, UA, AA, DA (1-fold), and Glu (10-fold). For further evaluating the selectivity of the proposed biosensor, metal ions and nitrite interfering substances such as NO_2^-, K^+, Zn^{2+}, Cr^{3+}, Pb^{2+}, and Cu^{2+} were investigated on the $ZnMn_2O_4$@rGO/GCE. As shown in Figure S4, when the same concentrations of interferences were injected, no obvious current response was observed. Accordingly, the result demonstrates that the $ZnMn_2O_4$@rGO has excellent selectivity performance.

The stability of $ZnMn_2O_4$@rGO/GCE was evaluated with addition of 0.5 mM H_2O_2 in 0.2 M NaOH as well. Figure 6d displays that the current response remained stable during 1000 s, which reveals stability of the proposed sensor. For reproducibility experiment, CVs were recorded by detecting 0.5 mM H_2O_2 with five different GCEs under the same condition. As indicated from Figure S5, the relative standard deviation was 3.1%, revealing good reproducibility of the fabricated biosensor.

3.5. Detecting H_2O_2 Released from MCF-7. H_2O_2, a major reactive oxygen species, is intimately related to signal transduction, aging, and cell proliferation.[57] Excessive concentration of H_2O_2 may cause numerous types of body dysfunction, including many different diseases and cancers of the human central nervous system.[58−60] Therefore, detection of extracellular H_2O_2 released from biological cells has turned out to be a hotspot. Zhu et al. reported a PtW/MoS_2 nanocomposite-modified electrode, exhibiting an ultrasensitive response to H_2O_2 reduction from breast cancer 4T1 cells (a mouse breast cancer cell line).[61]

MCF-7 cells as a common source of malignancies were adopted here for an in-depth study on the effectiveness of the determination of H_2O_2 from dysfunctional cells with the proposed biosensor. Before H_2O_2 detection, PMA was placed in the test solution, thereby stimulating H_2O_2 release from the MCF-7 cells.[62] Bright-field microscopy image of the MCF-7 is presented in Figure 7a. As seen in Figure 7b, amperometric curves were plotted when MCF-7 cells were absent or present with PMA and/or catalase added. When 6×10^6 cells mL^{-1} MCF-7 cells simulated by PMA were added in the test solution, the current increased rapidly with 20 nA for MCF-7 triggered by PMA. Nevertheless, when catalase was injected into the solution, the detectable response was negligible, suggesting that catalase decomposed the H_2O_2 from MCF-7 triggered by PMA. This phenomenon is well consistent with the literature.[63] Accordingly, the proposed sensor is applicable to assaying extracellular H_2O_2 released from MCF-7 cells, suggesting its remarkable potential in physiological and pathological applications.

4. CONCLUSIONS

In conclusion, $ZnMn_2O_4$@rGO microspheres have been prepared using a facile solvothermal technique, and their application in determination of H_2O_2 has been explored. The wrapped rGO improves the conductivity of $ZnMn_2O_4$ and further enhances its electrocatalysis toward H_2O_2 reduction. The $ZnMn_2O_4$@rGO/GCE exhibits a wider linear range and high sensitivity for the determination of H_2O_2. Furthermore, the proposed sensor can be employed to detect the extracellular H_2O_2 secreted by MCF-7 cells, revealing its tremendous potential for physiological and pathological applications.

■ ASSOCIATED CONTENT

Supporting Information

The Supporting Information is available free of charge at https://pubs.acs.org/doi/10.1021/acsami.9b19126.

https://dx.doi.org/10.1021/acsami.9b19126
ACS Appl. Mater. Interfaces 2020, 12, 3430−3437

Effect of temperature on calcinations, electrochemical kinetics of the $ZnMn_2O_4$@rGO/GCE, and optimization of sensing conditions (PDF)

AUTHOR INFORMATION

Corresponding Authors

Dongmei Deng − *Shanghai University, Shanghai, PR China*; Email: dmdeng@shu.edu.cn

Liqiang Luo − *Shanghai University, Shanghai, PR China*; orcid.org/0000-0002-5551-3861; Email: luck@shu.edu.cn

Other Authors

Yuanyuan Li − *Shanghai University, Shanghai, PR China*

Ke Huan − *Shanghai University, Shanghai, PR China*

Li Tang − *Shanghai University, Shanghai, PR China*

Jinhua Wang − *Shanghai University, Shanghai, PR China*

Complete contact information is available at: https://pubs.acs.org/10.1021/acsami.9b19126

Notes

The authors declare no competing financial interest.

ACKNOWLEDGMENTS

This work was supported by the National Natural Science Foundation of China (nos. 61571278, 61571280, and 61971274).

REFERENCES

(1) Izawa, S.; Kono, K.; Mimura, K.; Kawaguchi, Y.; Watanabe, M.; Maruyama, T.; Fujii, H. H_2O_2 production within tumor microenvironment inversely correlated with infiltration of CD56 NK cells in gastric and esophageal cancer: possible mechanisms of NK cell dysfunction. *Cancer Immunol. Res.* **2011**, *60*, 1801−1810.

(2) Youdim, K. A.; Joseph, J. A. A possible emerging role of phytochemicals in improving age-related neurological dysfunctions: a multiplicity of effects. *Free Radical Biol. Med.* **2001**, *30*, 583−594.

(3) Szatrowski, T. P.; Nathan, C. F. Production of large amounts of hydrogen peroxide by human tumor cells. *Cancer Res.* **1991**, *51*, 794−798.

(4) *Cancer Facts & Figures 2018*; American Cancer Society: Atlanta, 2018.

(5) Colditz, G. A.; Bohlke, K. Priorities for the primary prevention of breast cancer. *CA Cancer J. Clin.* **2014**, *64*, 186−194.

(6) Reuter, S.; Gupta, S. C.; Chaturvedi, M. M.; Aggarwal, B. B. Oxidative stress, inflammation, and cancer: how are they linked. *Free Radical Biol. Med.* **2010**, *49*, 1603−1616.

(7) Zhao, C.; Wu, X.; Li, P.; Zhao, C.; Qian, X. Hydrothermal deposition of CuO/rGO/Cu_2O nanocomposite on copper foil for sensitive nonenzymatic voltammetric determination of glucose and hydrogen peroxide. *Microchim. Acta* **2017**, *184*, 2341−2348.

(8) Nagaraja, P.; Prakash, J. S.; Asha, S. C.; Bhaskara, B. L.; Kumar, S. A. Dibenzazepin hydrochloride as a new spectrophotometric reagent for determination of hydrogen peroxide in plant extracts. *Environ. Monit. Assess.* **2012**, *184*, 5983−5988.

(9) Abo, M.; Urano, Y.; Hanaoka, K.; Terai, T.; Komatsu, T.; Nagano, T. Development of a highly sensitive fluorescence probe for hydrogen peroxide. *J. Am. Chem. Soc.* **2011**, *133*, 10629−10637.

(10) Luo, L.; Li, Q.; Xu, Y.; Ding, Y.; Wang, X.; Deng, D.; Xu, Y. Amperometric glucose biosensor based on $NiFe_2O_4$ nanoparticles and chitosan. *Sens. Actuators B* **2010**, *145*, 293−298.

(11) Liu, X.; Ye, D.; Luo, L.; Ding, Y.; Wang, Y.; Chu, Y. Highly sensitive determination of epinephrine by a MnO_2/Nafion modified glassy carbon electrode. *J. Electroanal. Chem.* **2012**, *665*, 1−5.

(12) Li, X.; Zhu, G.; Dou, J.; Yang, J.; Ge, Y.; Liu, J. Electrospun Au nanoparticle-containing ZnO nanofiber for non-enzyme H_2O_2 sensor. *Ionics* **2019**, *25*, 5527−5536.

(13) Cheng, X.; Zhang, J.; Chang, H.; Luo, L.; Nie, F.; Feng, X. High performance Cu/Cu_2O nanohybrid electrocatalyst for nonenzymatic glucose detection. *J. Mater. Chem. B* **2016**, *4*, 4652−4656.

(14) Yuan, K.; Ni, Y.; Zhang, L. Facile hydrothermal synthesis of polyhedral Fe_3O_4 nanocrystals, influencing factors and application in the electrochemical detection of H_2O_2. *J. Alloys Compd.* **2012**, *532*, 10−15.

(15) Ding, L.; Yan, J.; Zhao, Z.; Li, D. Synthesis of $NiGa_2O_4$ nanosheets for non-enzymatic glucose electrochemical sensor. *Sens. Actuators, B* **2019**, *296*, 126705−126710.

(16) Ngo, Y. L. T.; Sui, L.; Ahn, W.; Chung, J. S.; Hur, S. H. $NiMn_2O_4$ spinel binary nanostructure decorated on three-dimensional reduced graphene oxide hydrogel for bifunctional materials in non-enzymatic glucose sensor. *Nanoscale* **2017**, *9*, 19318−19327.

(17) Nithyayini, K. N.; Harish, M. N. K.; Nagashree, K. L. Electrochemical detection of nitrite at $NiFe_2O_4$ nanoparticles synthesised by solvent deficient method. *Electrochim. Acta* **2019**, *317*, 701−710.

(18) Balasubramanian, P.; Annalakshmi, M.; Chen, S. M.; Sathesh, T.; Peng, T. K.; Balamurugan, T. S. T. Facile Solvothermal Preparation of Mn_2CuO_4Microspheres: Excellent Electrocatalyst for Real-Time Detection of H_2O_2Released from Live Cells. *ACS Appl. Mater. Interfaces* **2018**, *10*, 43543−43551.

(19) Wu, Z.-L.; Li, C.-K.; Zhu, F.-W.; Liao, S.; Yu, J.-G.; Yang, H.; Chen, X. Q. Binary cobalt and manganese oxides: Amperometric sensing of hydrogen peroxide. *Sens. Actuators, B* **2017**, *253*, 949−957.

(20) Geim, A. K. Graphene: status and prospects. *Science* **2009**, *324*, 1530−1534.

(21) Rao, C. N. R.; Biswas, K.; Subrahmanyam, K. S.; Govindaraj, A. Graphene, the new nanocarbon. *J. Mater. Chem.* **2009**, *19*, 2457−2469.

(22) Wang, Y.; Shi, Z.; Huang, Y.; Ma, Y.; Wang, C.; Chen, M.; Chen, Y. Supercapacitor devices based on graphene materials. *J. Phys. Chem. C* **2009**, *113*, 13103−13107.

(23) Wei, P.; Gan, T.; Wu, K. N-methyl-2-pyrrolidone exfoliated graphene as highly sensitive analytical platform for carbendazim. *Sens. Actuators, B* **2018**, *274*, 551−559.

(24) Zhu, Y.; Murali, S.; Cai, W.; Li, X.; Suk, J. W.; Potts, J. R.; Ruoff, R. S. Graphene and graphene oxide: synthesis, properties, and applications. *Adv. Mater.* **2010**, *22*, 3906−3924.

(25) Cheng, G.; Liu, Y.-L.; Wang, Z.-G.; Zhang, J.-L.; Sun, D.-H.; Ni, J.-Z. The GO/rGO-Fe_3O_4 composites with good water-dispersibility and fast magnetic response for effective immobilization and enrichment of biomolecules. *J. Mater. Chem.* **2012**, *22*, 21998−22004.

(26) Ning, L.; Guan, X.; Ma, J.; Wang, M.; Fan, X.; Zhang, G.; Zhang, F.; Peng, W.; Li, Y. A highly sensitive nonenzymatic H_2O_2 sensor based on platinum, $ZnFe_2O_4$ functionalized reduced graphene oxide. *J. Alloys. Compd.* **2018**, *738*, 317−322.

(27) Zhang, J.; Rao, D.; Zheng, J. Synthesis of Ag nanoparticle doped MnO_2/GO nanocomposites at a gas/liquid interface and its application in H_2O_2 detection. *Electroanalysis* **2016**, *28*, 588−595.

(28) Kong, L.; Ren, Z.; Zheng, N.; Du, S.; Wu, J.; Tang, J.; Fu, H. Interconnected 1D Co_3O_4 nanowires on reduced graphene oxide for enzymeless H_2O_2 detection. *Nano Res.* **2015**, *8*, 469−480.

(29) Li, Y.; Tang, L.; Deng, D.; Ye, J.; Wu, Z.; Wang, J.; Luo, L. A novel non-enzymatic H_2O_2 sensor using $ZnMn_2O_4$ microspheres modified glassy carbon electrode. *Colloids Surf., B* **2019**, *179*, 293−298.

(30) Zhang, Y.; Deng, D.; Zhu, X.; Liu, S.; Zhu, Y.; Han, L.; Luo, L. Electrospun bimetallic Au-Ag/Co_3O_4 nanofibers for sensitive detection of hydrogen peroxide released from human cancer cells. *Anal. Chim. Acta* **2018**, *1042*, 20−28.

(31) Wang, D.; Zhou, W.; Zhang, Y.; Wang, Y.; Wu, G.; Yu, K.; Wen, G. A novel one-step strategy toward $ZnMn_2O_4$/N-doped graphene nanosheets with robust chemical interaction for superior lithium storage. *Nanotechnology* **2016**, *27*, No. 045405.

(32) Li, H.; Song, B.; Wang, W. J.; Chen, X. L. Facile synthesis, thermal, magnetic, Raman characterizations of spinel structure $ZnMn_2O_4$. *Mater. Chem. Phys.* **2011**, *130*, 39−44.
(33) Samanta, K.; Dussan, S.; Katiyar, R. S.; Bhattacharya, P. Structural and optical properties of nanocrystalline $Zn_{1-x}Mn_xO$. *Appl. Phys. Lett.* **2007**, *90*, 261903.
(34) Hadžić, B.; Romčević, N.; Romčević, M.; Kuryliszyn-Kudelska, I.; Dobrowolski, W.; Narkiewicz, U.; Sibera, D. Raman study of surface optical phonons in hydrothermally obtained ZnO(Mn) nanoparticles. *Opt. Mater.* **2016**, *58*, 317−322.
(35) Song, W.; Xie, J.; Liu, S.; Cao, G.; Zhu, T.; Zhao, X. Self-assembly of $ZnFe_2O_4$/graphene hybrid and its application as high-performance anode material for Li-ion batteries. *New J. Chem.* **2012**, *36*, 2236−2241.
(36) Kim, J. G.; Lee, S. H.; Kim, Y.; Kim, W. B. Fabrication of free-standing $ZnMn_2O_4$ mesoscale tubular arrays for lithium-ion anodes with highly reversible lithium storage properties. *ACS Appl. Mater. Interfaces* **2013**, *5*, 11321−11328.
(37) Biesinger, M. C.; Payne, B. P.; Grosvenor, A. P.; Lau, L. W. M.; Gerson, A. R.; Smart, R. S. C. Resolving surface chemical states in XPS analysis of first row transition metals, oxides and hydroxides: Cr, Mn, Fe, Co and Ni. *Appl. Surf. Sci.* **2011**, *257*, 2717−2730.
(38) Gu, X.; Yue, J.; Chen, L.; Liu, S.; Xu, H.; Yang, J.; Qian, Y.; Zhao, X. Coaxial MnO/N-doped carbon nanorods for advanced lithium-ion battery anodes. *J. Mater. Chem. A* **2015**, *3*, 1037−1041.
(39) Zhong, M.; Yang, D.; Xie, C.; Zhang, Z.; Zhou, Z.; Bu, X. H. Yolk−shell MnO@$ZnMn_2O_4$/N-C nanorods drived from α-MnO_2/ZIF-8 as anode materials for lithium ion batteries. *Small* **2016**, *12*, 5564−5571.
(40) Yuan, J.; Chen, C.; Hao, Y.; Zhang, X.; Agrawal, R.; Zhao, W.; Wang, C.; Yu, H.; Zhu, X.; Yu, Y.; Xiong, Z.; Xie, Y. Fabrication of three-dimensional porous $ZnMn_2O_4$ thin films on Ni foams through electrostatic spray deposition for high-performance lithium-ion battery anodes. *J. Alloys Compd.* **2017**, *696*, 1174−1179.
(41) Fan, B.; Hu, A.; Chen, X.; Zhang, S.; Tang, Q.; Wang, J.; Deng, W.; Liu, Z.; Xiao, K. Hierarchical Porous $ZnMn_2O_4$Microspheres as a High-Performance Anode for Lithium-Ion Batteries. *Electrochim. Acta* **2016**, *213*, 37−45.
(42) Rathnayake, R. M. N. M.; Wijayasinghe, H. W. M. A. C.; Pitawala, H. M. T. G. A.; Yoshimura, M.; Huang, H.-H. Synthesis of graphene oxide and reduced graphene oxide by needle platy natural vein graphite. *Appl. Surf. Sci.* **2017**, *393*, 309−315.
(43) Zhang, C.; Lv, W.; Xie, X.; Tang, D.; Liu, C.; Yang, Q.-H. Towards low temperature thermal exfoliation of graphite oxide for graphene production. *Carbon* **2013**, *62*, 11−24.
(44) Dreyer, D. R.; Todd, A. D.; Bielawski, C. W. Harnessing the chemistry of graphene oxide. *Chem. Soc. Rev.* **2014**, *43*, 5288−5301.
(45) Li, Y.; Zhang, Z.; Zhang, Y.; Deng, D.; Luo, L.; Han, B.; Fan, C. Nitidine chloride-assisted bio-functionalization of reduced graphene oxide by bovine serum albumin for impedimetric immunosensing. *Biosens. Bioelectron.* **2016**, *79*, 536−542.
(46) Cheng, K.; Yang, F.; Wang, G.; Yin, J.; Cao, D. Facile synthesis of porous $(Co, Mn)_3O_4$ nanowires free-standing on a Ni foam and their catalytic performance for H_2O_2 electroreduction. *J. Mater. Chem. A* **2013**, *1*, 1669−1676.
(47) Fu, Y.; Huang, D.; Li, C.; Zou, L.; Ye, B. Graphene blended with SnO_2 and Pd-Pt nanocages for sensitive nonenzymatic electrochemical detection of H_2O_2 released from living cells. *Anal. Chim. Acta* **2018**, *1014*, 10−18.
(48) Li, S.-J.; Xing, Y.; Yang, H.-Y.; Huang, J.-Y.; Wang, W.-T.; Liu, R.-T. Electrochemical synthesis of a binary Mn-Co oxides decorated graphene nanocomposites for application in nonenzymatic H_2O_2 sensing. *Int. J. Electrochem. Sci.* **2017**, *12*, 6566−6576.
(49) Ke, X.; Zhu, G.; Dai, Y.; Shen, Y.; Yang, J.; Liu, J. Fabrication of Pt-ZnO composite nanotube modified electrodes for the detection of H_2O_2. *J. Electroanal. Chem.* **2018**, *15*, 176−183.
(50) Zhao, X.; Li, Z.; Chen, C.; Wu, Y.; Zhu, Z.; Zhao, H.; Lan, M. A novel biomimetic hydrogen peroxide biosensor based on Pt flowers-decorated Fe_3O_4/graphene nanocomposite. *Electroanalysis* **2017**, *29*, 1518−1523.
(51) Achari, D. S.; Santhosh, C.; Deivasegamani, R.; Nivetha, R.; Bhatnagar, A.; Jeong, S. K.; Grace, A. N. A non-enzymatic sensor for hydrogen peroxide based on the use of α-Fe_2O_3 nanoparticles deposited on the surface of NiO nanosheets. *Microchim. Acta* **2017**, *184*, 3223−3229.
(52) Dou, J.; Zhu, G.; Hu, B.; Yang, J.; Ge, Y.; Li, X.; Liu, J. Wall thickness-tunable AgNPs-NCNTs for hydrogen peroxide sensing and oxygen reduction reaction. *Electrochim. Acta* **2019**, *306*, 466−476.
(53) Antink, W. H.; Choi, Y.; Seong, K.-d.; Piao, Y. Simple synthesis of CuO/Ag nanocomposite electrode using precursor ink for non-enzymatic electrochemical hydrogen peroxide sensing. *Sens. Actuators B* **2018**, *255*, 1995−2001.
(54) Shu, Y.; Chen, J.; Xu, Q.; Wei, Z.; Liu, F.; Lu, R.; Xu, S.; Hu, X. MoS_2 nanosheet-Au nanorod hybrids for highly sensitive amperometric detection of H_2O_2 in living cells. *J. Mater. Chem. B* **2017**, *5*, 1446−1453.
(55) Guo, Z.; Xu, J.; Zhang, J.; Hu, Y.; Pan, Y.; Miao, P. Facile strategy for electrochemical analysis of hydrogen peroxide based on multifunctional Fe_3O_4@Ag nanocomposites. *ACS Appl. Bio Mater.* **2018**, *1*, 367−373.
(56) Ramaraj, S.; Sakthivel, M.; Chen, S. M.; Lou, B. S.; Ho, K. C. Defect and additional active sites on the basal plane of manganese doped molybdenum diselenide for effective enzyme immobilization: In-vitro and in-vivo real time analysis for hydrogen peroxide sensing. *ACS Appl. Mater. Interfaces* **2019**, *11*, 7862−7871.
(57) Henzler, T.; Steudle, E. Transport and metabolic degradation of hydrogen peroxide in Chara corallina: model calculations and measurements with the pressure probe suggest transport of H_2O_2 across water channels. *J. Exp. Bot.* **2000**, *51*, 2053−2066.
(58) Luo, Y.; Liu, H.; Rui, Q.; Tian, Y. Detection of extracellular H_2O_2 released from human liver cancer cells based on TiO_2 nanoneedles with enhanced electron transfer of cytochrome c. *Anal. Chem.* **2009**, *81*, 3035−3041.
(59) Trachootham, D.; Alexandre, J.; Huang, P. Targeting cancer cells by ROS-mediated mechanisms: a radical therapeutic approach. *Nat. Rev. Drug Discovery* **2009**, *8*, 579−591.
(60) Veal, E.; Day, A. Hydrogen peroxide as a signaling molecule. *Antioxid. Redox Signaling* **2011**, *15*, 147−151.
(61) Zhu, L.; Zhang, Y.; Xu, P.; Wen, W.; Li, X.; Xu, J. PtW/MoS_2 hybrid nanocomposite for electrochemical sensing of H_2O_2 released from living cells. *Biosens. Bioelectron.* **2016**, *80*, 601−606.
(62) Wu, P.; Cai, Z.; Gao, Y.; Zhang, H.; Cai, C. Enhancing the electrochemical reduction of hydrogen peroxide based on nitrogen-doped graphene for measurement of its releasing process from living cells. *Chem. Commun.* **2011**, *47*, 11327−11329.
(63) Zhao, J.; Yan, Y.; Zhu, L.; Li, X.; Li, G. An amperometric biosensor for the detection of hydrogen peroxide released from human breast cancer cells. *Biosens. Bioelectron.* **2013**, *41*, 815−819.

https://dx.doi.org/10.1021/acsami.9b19126
ACS Appl. Mater. Interfaces 2020, 12, 3430−3437